Joint dynamic analysis of space manipulator with planetary gear train transmission

Tianfu Yang†, Shaoze Yan†*, Wei Ma‡
and Zengyao Han‡

† *State Key Laboratory of Tribology, Department of Mechanical Engineering, Tsinghua University, Beijing, 100084, China*
‡*China Academy of Space Technology, Beijing, 100094, China*

SUMMARY
Joints of space manipulators are usually simplified as torsional springs in modeling motion equations, and the nonlinear behaviors of the reducer in the joints are generally neglected. In this study, a dynamic model of a space manipulator that considers the joints that are transmitted through a typical 2K-H planetary gear reducer is developed using the Lagrangian method. The backlash clearances, gear tooth profile error, and time-variant meshing stiffness are integrated into the process. The simulation results show that the backlash clearances lead to the accumulation of positioning errors in the space manipulator when the joints rotate back and forth. The tooth profile error is the main cause of severe acceleration fluctuations and meshing force impacts. These fluctuations influence torque instability, which may accelerate gear system failure.

KEYWORDS: Robot dynamics; Space robotics; Manipulator joint; Planetary gear train; Backlash clearance; Tooth profile error.

1. Introduction
Precision robotic manipulators are widely used in the industrial, medical, and aerospace fields. Although these manipulators have been investigated for many decades, the accuracy of the modeling remains unsatisfactory under certain working circumstances.[1] Although some countries, such as Canada and Japan, have already launched space manipulators,[2] the precise modeling of these large-scale manipulators continues to be a challenge especially in the complex space environment.

Traditional research approaches focus on the flexibility of long robotic arms and ignore the influence of joints. The simplification of the manipulator joint modeling and the neglect for nonlinear factors result in an irrational and unpredictable manipulator response. Early studies have modeled these joints as ideal revolute hinges.[3] Komatsu *et al.*[4] constructed a two-link flexible SCARA manipulator system and studied the influence of arm deflection on positioning accuracy. Morris *et al.*[5] discussed the coupling and interactions between the links of a manipulator system as well as combined elastic and rigid link motions according to the superposition principle. He *et al.*[6] investigated joint clearance on the basis of ideal hinge. Nevertheless, all these models have neglected the importance of joint dynamics, which is a key to attaining accurate prediction of dynamic behaviors.

Joint errors in large-scale space manipulators are amplified, which results in a considerable tip-positioning inaccuracy. These errors will even accumulate for serial manipulators. Therefore, joint dynamics must be modeled precisely for large-scale serial space manipulators. In a study on the dynamic properties of SRMS, Nguyen *et al.*[7] pointed out that aside from arm flexibility, the flexibility of joint transmission components is a significant factor that influences system response.

Spong *et al.*[8] were the first to derive a simple elastic joint model of a robotic manipulator, which was significantly more tractable in terms of controller design compared with previous nonlinear

---

* Corresponding author. E-mail: yansz@mail.tsinghua.edu.cn
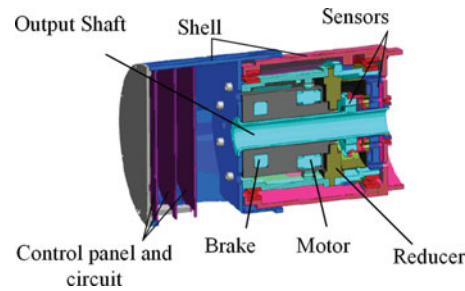
Fig. 1. A typical space manipulator joint.

models that were used for elastic joint manipulators. Ghorbel *et al.*[9] developed an adaptive control method with a simple correction term for joint elasticity based on the theory of Spong *et al.* Korayem *et al.*[10] compared the effects of flexibility on the maximum and rigid payload values. Simulation was performed on a rigid-joint three-link manipulator, and a reasonable agreement was observed. Salmisi *et al.*[11] designed a controller with a friction-compensating torque based on the torsional spring model. Liu *et al.*[12] modeled a cubic model friction in joints. Ciliz[13] and Subudhi *et al.*[14] also developed novel control strategies based on the torsional spring model. Zhao *et al.*[15−17] and Wang *et al.* investigated a redundant manipulator with linear spring elastic joints, which demonstrated rich dynamic behaviors. Gan *et al.*[18] introduced a 3-DOF serial manipulator model that considered reducer and actuator compliance as well as proposed a stiffness design method to protect the actuator. However, the configuration of the reducer was incomplete, which could pose problems because the joint configuration is more complicated in an actual space manipulator. A typical space manipulator joint comprises a servo motor, reducer, bearings, sensors, and circuit (Fig. 1), among which the reducer is a major transmission component that affects the dynamic properties. The joint dynamic model must be more complex and take the reducers into account, particularly when the transmission reduction ratio of a large-scale manipulator is considerably high, to guarantee low-speed operation stability.[19]

Du *et al.*[20] considered the friction, backlash, and hysteresis of harmonic gearing in their model, which effectively reflected the nonlinear features of robot joints. Thus, the model can be used to describe the characteristics and to improve the accuracy of the modeling of robot joints. Aside from harmonic gearing, planetary gear train is a major type of reducer that is often used in space manipulator joints. The former is usually installed in light robotic manipulators, whereas the latter is installed in large and heavy-duty robotic manipulators. However, investigations on the influence of planetary gear reducer on robotic manipulators have been minimal.[21] A planetary gear train is a complex system that includes multiple pairs of meshing teeth during transmission. The micro meshing displacements are coupled with the rotation of rigid links and may produce unexpected effects on the dynamic behaviors of the manipulators.

A coupled model of two-link planar manipulators that are transmitted through a 2K-H planetary gear train is developed in this study. First, the modeling method of nonlinear factors, backlash clearance, tooth profile error, and time-variant stiffness is presented. Subsequently, the dynamic equations of the space manipulator system are derived using the Lagrangian method. Second, numerical simulations are performed to predict the dynamic characteristics of the space manipulator. Finally, the effects of some nonlinear parameters, such as backlash clearance and tooth profile error, on the dynamic behaviors of the manipulator are analyzed. By performing a simulation analysis, the positioning errors that accumulate when joints rotate back and forth have been identified as the main cause of severe acceleration fluctuations and meshing force impacts.

2. Dynamic Modeling
A typical two-link space manipulator mounted on a space craft is presented in Fig. 2. The ideal dynamic model for the manipulator comprises a shoulder joint, elbow joint, main arms, and small fine arms. Given that this study primarily analyzes the main arm joints, the links are modeled as rigid bodies. Moreover, given that the manipulator is used in gravity-free environment, gravity is neglected.
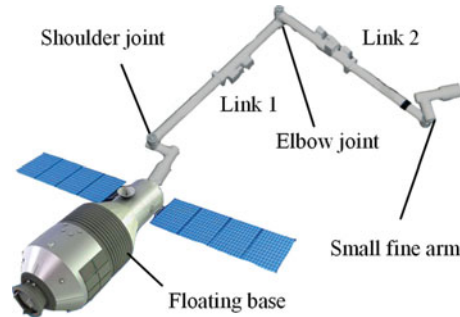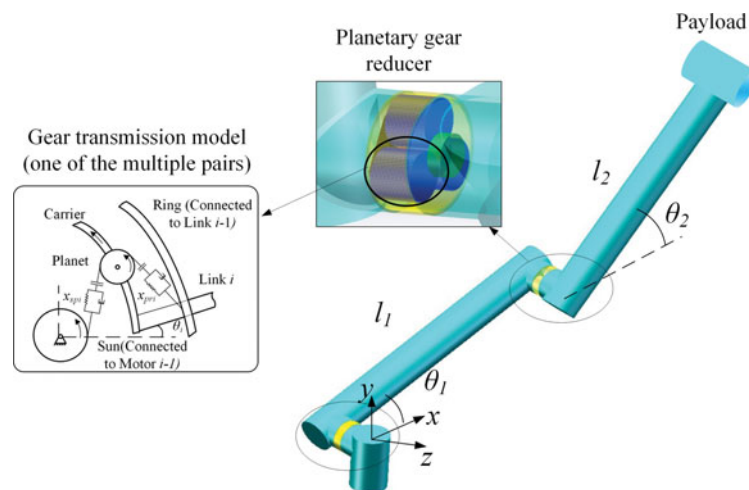
Fig. 2. A space manipulator on a space craft.

Fig. 3. Flexible joint model that integrates a gearbox.

The mass of the floated base is larger than that of the manipulator, which indicates that the movement of the base is not obvious. Therefore, a fixed base is hypothesized. The dynamic equation of a typical rigid link manipulator is expressed as follows:

$$\mathbf{M\ddot{q}} + [\mathbf{C(q, \dot{q})} + \mathbf{D}] \cdot \dot{\mathbf{q}} = \mathbf{T}, \tag{1}$$

where $\mathbf{M}$ denotes the inertia matrix of links, $\mathbf{C(q, \dot{q})}$ denotes the Coriolis forces and the centripetal forces matrix, and $\mathbf{D}$ denotes the damping matrix. The rigid model is used as the basis for the detailed manipulator model that is transmitted through the planetary gear trains. Simulation is performed to compare the model with the detailed model with planetary gear trains.

The detailed model considers the configuration of the planetary gear trains. A typical driving unit with 2K-H planetary gearbox is shown in Fig. 3. The motor shaft is rigidly connected to the input side of gearbox, and the output side is also rigidly attached to the link. The planetary gear train comprises a sun gear, three planet gears, a ring gear, and a carrier. The reduction ratio depends on the number of teeth. As a reducer, the ring gear must be fixed and the sun gear must work as an input shaft for the carrier to deliver a reduction rotation in the reduction ratio of $n = z_r/z_s + 1$, where z_r and z_s represent the gear tooth number of the ring and sun gears, respectively.

During the modeling of the gearbox, we assumed that all of the gears are spur gears, that the three plant gears have the same material, size, and other structural parameters, and that the influence of the gear on gear friction and lubrication is negligible.

Several nonlinear effects, such as backlash clearance, tooth profile error, and time-variant meshing stiffness, are considered in the planetary gear train model. The modeling method is described in the following sections.

2.1. Backlash clearance

The backlash clearance ensures the proper assembly of gears or identifies the need to modify the gears. Given that the clearance effect is neglected in most models, the effect and inaccuracy from the backlash are omitted. The rotation is transmitted via gear meshing, and the meshing contact forces are modeled as linear springs. The spring force becomes a nonlinear factor when the backlash is considered. The existence of backlash clearances discontinues the meshing force and excites fluctuation, which may eventually result in instability. The planetary gearbox consists of multiple pairs of gears that are meshing simultaneously, which exacerbates the effect of backlash clearances. Therefore, the meshing clearance cannot be ignored in the modeling of the planetary gear train.

The rotations must be converted into linear displacements in meshing lines to enable the calculation of the meshing force. The following equation is used:

$$\begin{cases} x_s = r_s\theta_s \\ x_p = r_p\theta_p \\ x_c = r_c\theta_c\cos\alpha \end{cases}, \tag{2}$$

where r_s and r_p denote the base radii of the sun and planet gears, respectively, r_c denotes carrier radius, θ_s, θ_p, and θ_c are the rotational angles of the sun gear, planet gear, and carrier, respectively, and α refers to the meshing pressure angle.

During the meshing process, the gear tooth surface generates a micro deformation and the displacements of the meshing pair begin to deviate. Let the error of the displacements between the meshing be expressed as follows:

$$\begin{cases} x_{sp} = x_s - x_p - x_c \\ x_{pr} = x_p - x_c \end{cases}, \tag{3}$$

where the subscripts *sp* and *pr* represent the errors between the sun and planet gears and between the planet and ring gears, respectively.

As mentioned above, the meshing forces are modeled as nonlinear springs. The meshing forces for the meshing pairs with a backlash clearance of 2*b* are expressed as follows:

$$\begin{cases} F_{sp} = k_{sp}(t) \cdot f_k(x_{sp}, b) \\ F_{pr} = k_{pr}(t) \cdot f_k(x_{pr}, b) \end{cases}, \tag{4}$$

where $k(t)$ is the stiffness coefficient and $f_k(x, b)$ is a piecewise linear function that simulates a backlash clearance effect, which in turn is computed as follows:

$$f_k(x, b) = \begin{cases} x - b & x > b \\ 0 & -b < x \le b \\ x + b & x \le -b \end{cases}. \tag{5}$$

The use of Eq. (5) is inconvenient for numerical calculation. The function is used repeatedly during the calculation, which significantly extends the calculation time. The discontinuous points may lead to divergence and result in the failure of the numerical solution. The function is usually replaced by another function that is composed of hyperbolic tangent functions, which is expressed as follows:

$$f_k(x, b) = x + \frac{x}{2}[\tanh(\sigma \cdot (x - b)) - \tanh(\sigma \cdot (x + b))]$$

$$- \frac{b}{2}[\tanh(\sigma \cdot (x - b)) + \tanh(\sigma \cdot (x + b))], \tag{6}$$

where σ is a parameter that adjusts the shape of the function curve. As illustrated in Fig. 4, the approximation is sufficiently accurate when σ is large enough.
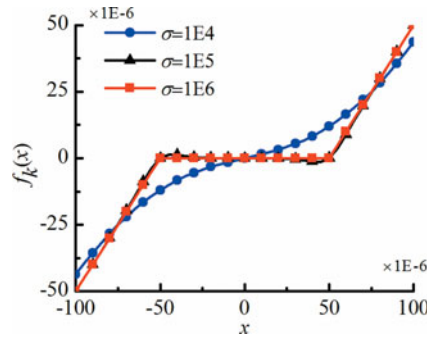
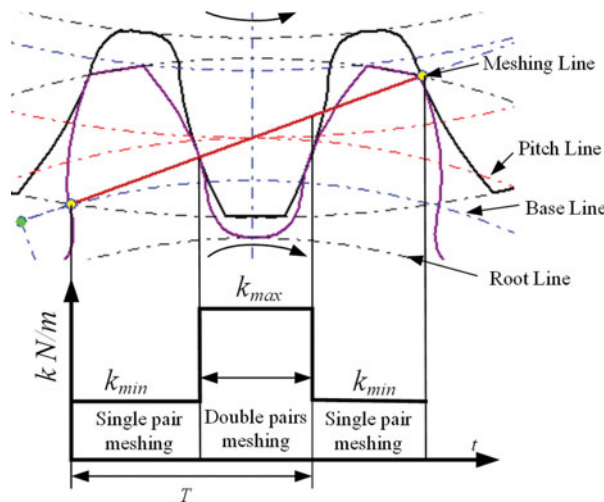Fig. 4. Clearance function of *tanh* with different σ.

Fig. 5. Time-variant stiffness.

2.2. Time-variant meshing stiffness

Meshing stiffness $k(t)$ in Eq. (4) is time variant because the number of pairs and their equivalent stiffness varies throughout the meshing period. The meshing force increases when multiple pairs of teeth are involved in the meshing, but decreases when only a single pair of teeth is used. The time-variant stiffness also acts as the fluctuation motivation of the system, which must also be considered in the dynamic modeling.

In most of the cases where a pair of gears has a contact ratio of less than 2, the meshing stiffness of the spur gear is simplified as a square wave as shown in Fig. 5. k_{max} is the meshing stiffness with double pairs of teeth meshing, k_{min} is the meshing stiffness with a single pair of teeth meshing, T denotes the meshing period, γ is the phase difference among various pairs, and e denotes the contact ratio.

The meshing stiffness is processed via Fourier transform, which is expressed as follows:

$$k = k_{\min} + (k_{\max} - k_{\min})(e-1) + \sum_{i=1}^{n} \frac{k_{\max} - k_{\min}}{i\pi} \left[\sin 2\pi i \left(e - 1 - \frac{t}{T} \right) + \sin 2\pi i \left(\frac{t}{T} \right) \right]. \quad (7)$$

For the convenience, the high-frequency components are ignored and only the fundamental frequency component is deemed sufficient for time-variant stiffness estimation. The meshing stiffness is expressed as follows:

$$k(t) = k_m + k_a \sin(\omega_e t), \quad (8)$$

where k_m denotes the mean meshing stiffness, k_a denotes the time-variant meshing stiffness, and ω_e denotes the meshing circle frequency.

The meshing circle frequency is determined by the rotational speed and the tooth number of the meshing pair as expressed in the following equation:

$$\omega_e = \omega z, \tag{9}$$

where ω denotes the circular frequency of the specified gear and z denotes its tooth number. Two types of meshing exist in a planetary gearbox, namely, sun-planet meshing and ring-planet meshing. By hypothesizing that the carrier is fixed and that the ring gear is rotational, both pairs of meshing become fixed-axis gear trains. In the actual system, ω should be transformed into the relative circular frequency between the specified gear and the carrier. Therefore, the actual meshing circular frequency is expressed as follows:

$$\omega_{ie} = (\omega_i - \omega_c) z_i, \quad i = s, p, r. \tag{10}$$

By taking the sun gear as example, we substitute x_{sp}, x_{pr}, and $\dot{\theta}_c$ into Eq. (10) and evaluate rotational circular frequency as follows:

$$\omega_{spe} = \left(\frac{\dot{x}_{sp} + \dot{x}_{pr} + 2\dot{\theta}_c r_c cos\alpha}{r_s} - \dot{\theta}_c \right) z_s, \tag{11}$$

where $\dot{x}_{sp}$ and $\dot{x}_{pr}$ are several orders of magnitude less than $\dot{\theta}_c$ and thus, are ignorable in Eq. (11). Therefore, the rotational circular frequency of the sun-planet meshing circular frequency is expressed as follows:

$$\omega_{spe} = \dot{\theta}_c z_s \left(\frac{2r_c cos\alpha}{r_s} - 1 \right). \tag{12}$$

Similarly, the ring-planet meshing circular frequency is expressed as follows:

$$\omega_{pre} = \dot{\theta}_c z_p \left(\frac{r_c cos\alpha}{r_p} - 1 \right). \tag{13}$$

2.3. Tooth profile error

Tooth profile error is the summation of the deviation between the actual tooth profile and the correct involute curve that passes through the pitch point that is measured perpendicular to the actual profile. The causes of the tooth error are diverse, such as the misalignment of work pieces, the inaccurate profile of the cutting tool, and the inappropriate machining process, which are unavoidable during the manufacturing process. Although improving the machining precision will reduce the tooth profile error, such improvement is limited and the advancement of the precision grade inevitably increases the manufacturing costs. Therefore, if the error is modeled accurately in the dynamic model, the influence of such error can be avoided.

This kind of error is also time variant and related to the meshing frequency. The deviation is also capable of exciting the fluctuation in the meshing process. When analyzing gear dynamics, the gear meshing error is usually decomposed into Fourier series because the time-variant stiffness neglects the high-order components to maintain the convenience of numerical calculation of the fundamental component.

$$e(t) = E \sin(\omega_e t), \tag{14}$$

where E denotes the error magnitude that is determined by the machining precision requirement. The meshing circular frequency ω_e is similar to time-variant stiffness, which is calculated in Eq. (10). Thus, the meshing forces can be expressed as follows:

$$\begin{cases} F_{spi} = k_{spi}(t) \cdot (x_{spi} - e_{spi}(t)) \\ F_{pri} = k_{pri}(t) \cdot (x_{pri} - e_{pri}(t)) \end{cases}. \tag{15}$$

2.4. Dynamic equations

After deriving the nonlinear factors in the gear train, the detailed dynamic model of the two-link manipulator becomes accessible. The detailed model is derived using the Lagrangian method. The kinetic energy of each link and joint is calculated.

The kinetic energy of the shoulder joint is computed as follows:

$$T_{j1} = \frac{1}{2}I_{s1}\dot{\theta}_{s1}^2 + \frac{3}{2}I_{p1}\dot{\theta}_{p1}^2 + \frac{1}{2}\left(I_{c1} + 3m_{p1}r_{c1}^2\right)\dot{\theta}_1^2. \tag{16}$$

The kinetic energy of link-1 is computed as follows:

$$T_{L1} = \frac{1}{2}\left(I_1 + m_1 d_1^2\right)\dot{\theta}_1^2 + \frac{1}{2}m_j L_1^2 \dot{\theta}_1^2. \tag{17}$$

The kinetic energy of the elbow joint is computed as follows:

$$T_{j1} = \frac{1}{2}I_{s2}(\dot{\theta}_1 + \dot{\theta}_{s2})^2 + \frac{3}{2}I_{pi2}\dot{\theta}_{pi2}^2 + \frac{1}{2}\left(I_{c2} + 3m_{p2}r_{c2}^2\right)(\dot{\theta}_1 + \dot{\theta}_2)^2. \tag{18}$$

The kinetic energy of link-2 with payload is computed as follows:

$$T_{L2} = \frac{1}{2}I_2\left(\dot{\theta}_1 + \dot{\theta}_2\right)^2 + \frac{1}{2}m_2\left\{\left[L_1\dot{\theta}_1\cos\theta_2 + (\dot{\theta}_1 + \dot{\theta}_2)d_2\right]^2 + \left(L_1\dot{\theta}_1\sin\theta_2\right)^2\right\}$$
$$+ \frac{1}{2}m_p\left\{\left[L_1\dot{\theta}_1\cos\theta_2 + (\dot{\theta}_1 + \dot{\theta}_2)L_2\right]^2 + \left(L_1\dot{\theta}_1\sin\theta_2\right)^2\right\}, \tag{19}$$

where the single and double dots represent the first and second derivatives, respectively, with respect to time. The subscripts *si, pi,* and *ci* denote the sun gear, planet gear, and carrier of the *i*th joint, respectively. θ_1 and θ_2 denote the output angles of the shoulder and elbow joints, respectively, which are rigidly attached to the carriers. Therefore, these variables also represent the rotational angle of the carriers. The other parameters are similarly defined as the rigid model parameters.

Gravity force is neglected because the manipulator is in orbit. Given that spring potential energy is included in the nonlinear meshing force, no other potential energy needs to be calculated. This model represents a large gross motion and a small elastic deformation of the gear teeth coupling system. In order to analyze both the rigid angular movement and the fluctuation characteristics conveniently, generalized coordinates are set as linear displacement errors in the meshing line and in the rotational angle of both joints as shown in the following equation:

$$\mathbf{q} = [\, x_{sp1}\ x_{pr1}\ \theta_1\ x_{sp2}\ x_{pr2}\ \theta_2 \,]^T. \tag{20}$$

By substituting Eqs. (16) to (19) into the Lagrangian equations, the final dynamic model of the manipulator system can be summarized as follows:

$$\mathbf{M(q)\ddot{q}} + [\mathbf{C(q, \dot{q})} + \mathbf{D}]\,\dot{\mathbf{q}} = \mathbf{F(q, \dot{q})}, \tag{21}$$

where $\mathbf{M(q)}$ denotes the inertia matrix, $\mathbf{C(q, \dot{q})}$ denotes the velocity quadratic coupling matrix, $\mathbf{D}$ denotes the diagonal positive definite damping matrix, and $\mathbf{F(q, \dot{q})}$ denotes the generalized force vector. The elements in the matrixes and vectors of Eq. (21) are listed below, whereas the other unlisted elements are equal to zero:

$M_{11} = M_{s1}, M_{12} = M_{21} = M_{s1}, M_{13} = M_{31} = 2M_{s1}r_{c1p},$

$M_{22} = M_{s1} + 3M_{p1}, M_{23} = M_{32} = (2M_{s1} + 3M_{p1})r_{c1p};$

$M_{33} = a_{11} + a_2 + M_{s2}r_{c1p}^2 + a_3 + 2a_4\cos\theta_2, M_{34} = M_{43} = M_{s2}r_{c1p}, M_{35} = M_{53} = M_{s2}r_{c1p},$

$M_{36} = M_{63} = 2M_{s2}r_{s2}r_{c2p} + a_3 + a_4\cos\theta_2, M_{44} = M_{45} = M_{54} = M_{s2}, M_{46} = M_{64} = 2M_{s2}r_{c2p},$

$M_{55} = M_{s2} + 3M_{p2}, M_{56} = M_{65} = (2M_{s2} + 3M_{p2})r_{c2p}, M_{66} = a_{12} + a_3;$

$C_{33} = -2a_4 \sin\theta_2 \cdot \dot{\theta}_2, C_{36} = -a_4 \sin\theta_2 \cdot \dot{\theta}_2, C_{63} = a_4 \sin\theta_2 \cdot \dot{\theta}_1;$

$r_{cip} = r_c \cos\alpha, I_{cip} = I_{ci} + 3m_{pi}r_{ci}^2 + I_i, M_{si} = I_{si}/r_{si}^2, M_{pi} = I_{pi}/r_{pi}^2, M_{ci} = I_{ci}/r_{cip}^2, (i = 1, 2),$

$m_j = m_{s2} + 3m_p + m_{c2} + m_{r2}, a_{1i} = (4M_{si} + 3M_{pi})r_{cip}^2, a_2 = I'_{c1} + m_1 d_1^2 + (m_2 + m_j + m_p)L_1^2,$

$a_3 = I'_{c2} + m_2 d_2^2 + m_p L_2^2, a_4 = L_1 \cdot a_6, a_5 = m_1 d_1 + (m_2 + m_j + m_p)L_1, a_6 = m_2 d_2 + m_p L_2.$

where l denotes arm length and d denotes the arms' center of mass position. Subscripts 1 and 2 represent the first and second arms, respectively, z denotes the gear tooth number, and m denotes mass, which is computed as $M = J/r^2$, where J and r denote the rotary inertia and radius of gears, respectively. The subscripts $s, p, c,$ and r correspond to sun gear, planet gear, carrier, and ring gear, respectively.

The meshing force and driving torque are modeled as a generalized force $\mathbf{F}(\mathbf{q}, \dot{\mathbf{q}})$ that is derived based on the virtual work principle. Some generalized coordinates are considered as translational displacements in the meshing line, and the driving torque is coupled with all the generalized coordinates. The torque must be converted into force in the meshing lines. By substituting Eq. (15) and driving torque T_1 and T_2 into the dynamic equation, the generalized force vector can be written as follows:

$$F = \begin{bmatrix} -3F_{sp1} + T_1/r_{s1} \\ -3F_{pr1} + T_1/r_{s1} \\ 2T_1 r_{c1p}/r_{s1} \\ -3F_{sp2} + T_2/r_{s2} \\ -3F_{pr2} + T_2/r_{s2} \\ 2T_2 r_{c2p}/r_{s2} \end{bmatrix}. \tag{22}$$

The dynamics of the manipulator is simulated based on the derived model. Numerical integration is performed with a fourth-order Runge-Kutta algorithm. The numerical simulations are performed on a Xeon E5620 workstation. The results are presented in the next section.

3. Dynamic Simulations
In order to determine the influence of the planetary gear train, the rigid model is simulated under the same payload and driving conditions that are mentioned above. The results of the rigid model are used as a 'baseline' for the comparison with the detailed model. Owing to the torque amplitude effect of the reduction gearbox, the output torque that is loaded on the link is amplified by the N (reduction ratio) times. Therefore, the torque mentioned in the following sections refers to the torque in the rigid model. The torque of the detailed model must be divided by the reduction ratio.

The starting positions of the joints are set to zero, the displacement error of the gear pairs must be out of contact or just initiating contact provided that the displacement error of the gear pairs is out of contact or just beginning to make contact. The initial velocities are set to zero. Therefore, the initial values for the detailed model are set to $[b\ b\ 0\ b\ b\ 0\ 0\ 0\ 0\ 0\ 0\ 0]^T$, whereas the initial values for the rigid model are set to zero.

The other parameters that are used in this section are listed in Table I. a_1 and a_2 denote the cross-sectional area of arms, ρ_{link} denotes the density of arms, and m_{payload} denotes the payload mass. The other parameters have been defined in the preceding paragraphs.

3.1. Constant torque driving response
A constant driving torque of 100 Nm is loaded on both joints at 0.5 s. The output angular displacement deviation $\Delta\theta$ and velocity deviation $\Delta\omega$ from the rigid and detailed models are illustrated in Figs. 6 and 7, respectively. The errors appear tolerable compared with those of the half-circle working stroke of arm. Nevertheless, given that the length of the links is of meter degree, a 0.02 rad deviation of the first link and a 0.01 rad deviation of the second link will result in an approximately 30 mm

Table I. Simulation parameters ($i = 1,2$).

Parameters	Value	Unit	Parameters	Value	Unit	Parameters	Value	Unit
l_1	1	m	z_r	99		M_{ci}	5.8	kg
l_2	0.7	m	m	3	mm	M_{ri}	10	kg
d_1	0.5	m	b	50	μm	m_{si}	0.39	kg
d_2	0.35	m	α	24.6	°	m_{pi}	0.61	kg
a_1	0.01	m^2	k_m	1e8	N/m	m_{ci}	6.29	kg
a_2	0.01	m^2	k_a	2e7	N/m	ρ_{link}	2700	kg/m^3
z_s	27		M_{si}	0.5	kg	E	5	μm
z_p	36		M_{pi}	0.66	kg	$m_{payload}$	10	kg
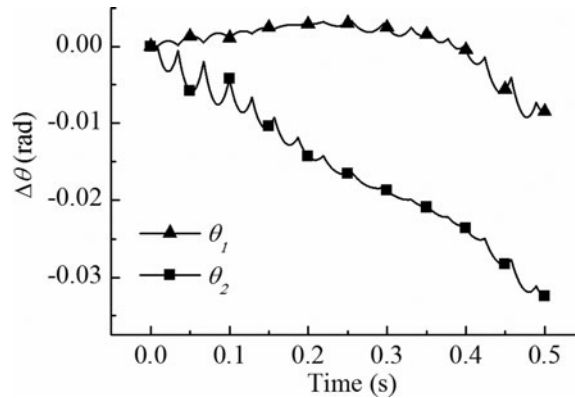
Fig. 6. Angular displacements that are driven by constant torque.
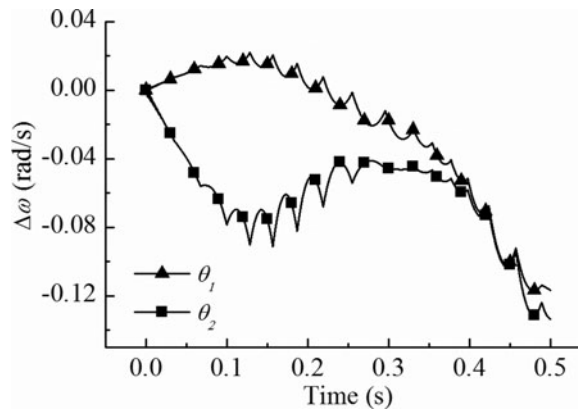
Fig. 7. Angular velocities that are driven by constant torque.

tip-positioning inaccuracy, which is deemed considerable under specific precision positioning control circumstances. Moreover, these errors accumulate over time, which makes the model suitable for long-time, long-stroke work.,

Figures 8 and 9 show the sun-planet meshing displacement error x_{sp1} and force F_{sp1}, respectively. Given that the results of the other pairs follow the same trend, the abovementioned pair is taken as an example. The displacement error x_{sp1} vibrates at the beginning and then rapidly converges to $52\,\mu$m. The same trend is demonstrated by the meshing force F_{sp1}, which is caused by the starting impact when the gear pairs begin to approach each other (Fig. 9). The fluctuation of x_{sp} that follows is caused by the tooth profile error because the magnitude is approximately $10\,\mu$m, which is similar to that of the given tooth error. The frequency increases over time because the rotational velocity of the shoulder joint increases and the tooth error is related to the joint velocity. As expected, the dynamic response of the detailed model shows a slight difference with that of the rigid model and gear mesh behavior. Thus, the system dynamic equations are validated.
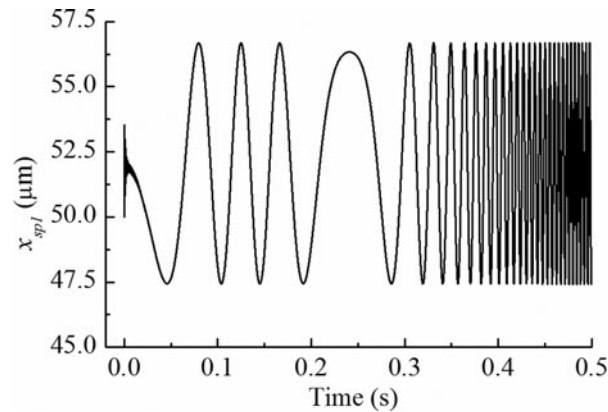
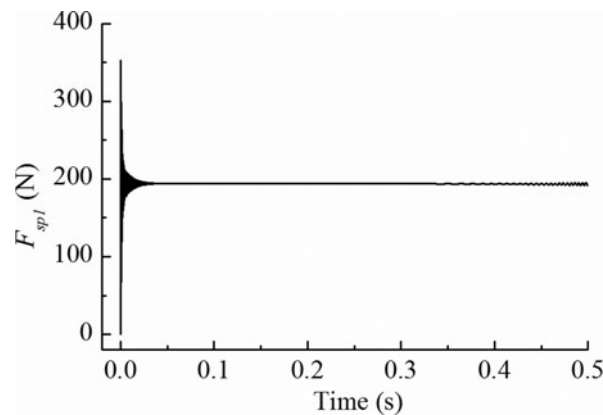Fig. 8. Sun-planet meshing displacement error of the shoulder joint.

Fig. 9. Sun-planet meshing force of the shoulder joint.

3.2. PD control response

The manipulator is rarely driven by constant torque in an actual space manipulator system. The manipulator is commonly used to reach a certain position. In this section, the manipulator is simulated to rotate 30 degrees for θ_1 and θ_2. The driving torque is controlled using the regular PD controlling method. For both joints to rotate 30 degrees, the controlling torque is set as follows:

$$T_i = P \cdot \left(\frac{\pi}{6} - \theta_i\right) - D \cdot \dot{\theta}_i \ (i = 1, 2). \tag{23}$$

The angular displacements of θ_1 and θ_2 with different proportional and differential gains are illustrated in Fig. 10. A proportional gain of $P = 1000$ and a differential gain of $D = 400$ are deemed suitable to drive the manipulator to its desired position without generating considerable overshoot. Therefore, the following analyses are all based on this set of parameters. As illustrated in Fig. 10, both θ_1 and θ_2 go up directly to 30 degrees and stabilize after 2.6 s. The angular displacement does not fluctuate in the process. However, the driving torque of both joints fluctuates in high frequency during the process as shown in Fig. 11. Therefore, the angular displacement error can be eliminated using the closed-loop controlling method, which requires the high-frequency response of the servo motor to ensure a stable output displacement. Given that the motor torque fluctuation follows the same trend as that of the angular acceleration in Fig. 14, the following fluctuation analysis is based on acceleration to reflect the motor torque fluctuation indirectly.

The angular acceleration of the shoulder joint shows severe fluctuations in Fig. 14. The acceleration of the 'baseline model' is plotted with dashed line that corresponds to the Y axis on the right, whereas the acceleration of the rigid model is plotted with solid line that corresponds to the Y axis on the left. In all three instances of fluctuation, the acceleration is occasionally reduced to zero, which means that the gear pairs are in a non-contact situation.
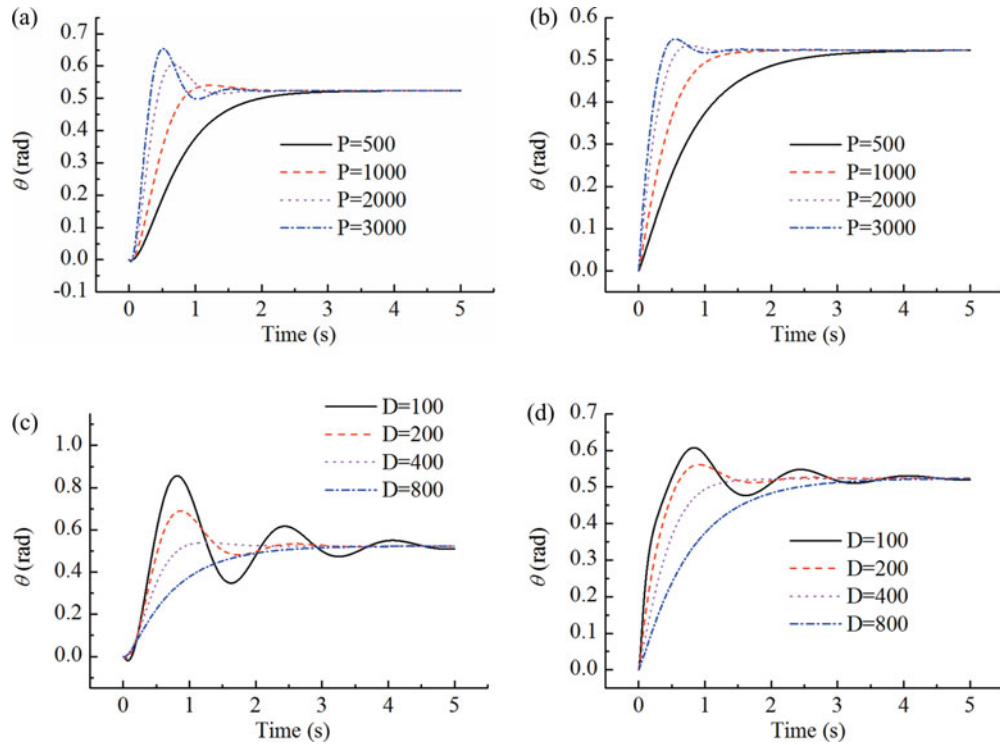
Fig. 10. Angular displacements with different proportional and differential gains. (a) Shoulder joint angular displacements with different proportional gains. (b) Elbow joint angular displacements with different proportional gains. (c) Shoulder joint angular displacements with different differential gains. (d) Elbow joint angular displacements with different differential gains.
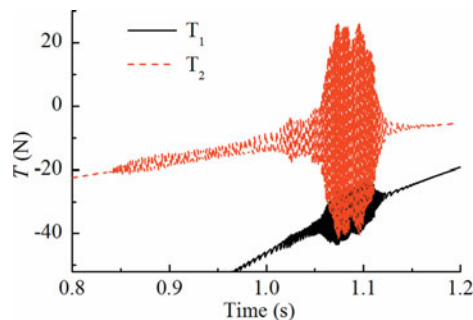

Fig. 11. PD-controlling driving torques.

The first fluctuation is excited by the starting impact. Based on the meshing displacements and forces in Figs. 12 and 13, the second fluctuation occurs when the meshing displacement error and force change their signs after 0.3 s, which indicates that the gear pairs are meshing on the opposite side. The sudden change in meshing displacement is caused by the backlash clearance. The velocity gradually decreases to zero when the gear pair returns to its origin side in 1.5 s, which produces the fourth fluctuation, one that is smaller than the previous three fluctuations. Given that the first three fluctuations are all excited by the meshing impact, these cannot converge quickly because of the effect of gear teeth deformation damping. However, the third fluctuation does not occur after sudden excitations and shows a trend of instability. This fluctuation, which is deemed as a self-excited vibration, may be attributed to the tooth profile error and time-variant stiffness. The maximum value of the acceleration deviation of the first two fluctuations ranges between 10 rad/s^2 and 40 rad/s^2, whereas that of the third fluctuation reaches up to 300 rad/s^2, which indicates that the fluctuation caused by internal excitation is more severe than the fluctuation caused by the normal gear pair meshing impact.
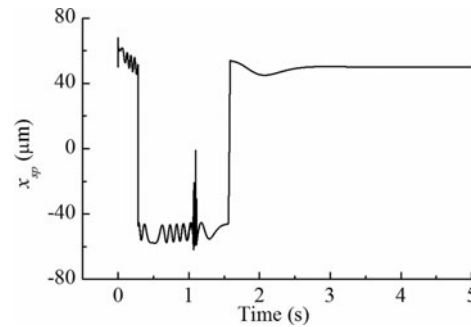
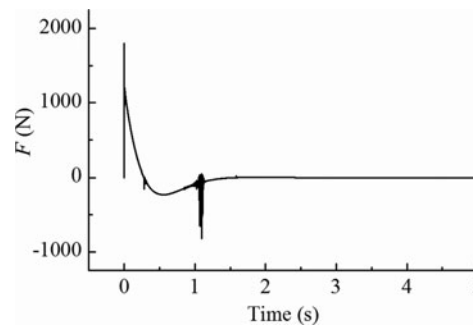Fig. 12. Sun-planet meshing displacement of the shoulder joint.

Fig. 13. Sun-planet meshing force of the shoulder joint.

The detailed manipulator model with the planetary gear train presents richer phenomena. Although backlash clearance and tooth error have limited influence on positioning accuracy, these factors cause a considerable acceleration fluctuation. The models that neglect one of these three nonlinear factors are also calculated to verify the main cause of the fluctuations. The second fluctuation disappears and the third fluctuation is amplified when the backlash clearance is neglected, which conforms to the inference that the second fluctuation is caused by the gear pairs that turn to the opposite meshing side. The third fluctuation vanishes when tooth error is neglected, and all three fluctuations occur, with the third fluctuation having a lesser magnitude, when time-variant stiffness is neglected. Therefore, tooth error is the main source of internal excitation, whereas time-variant stiffness is the cause of the intensification of the fluctuation magnitude. The tiny clearance and manufacturing error will generate an evident fluctuation of rational acceleration and result in an uncontrollable output velocity.

4. Parametric Analysis

The dynamic model of the manipulator is complex, and the effects of different nonlinear factors are difficult to distinguish. The fluctuations that are caused by the starting and meshing impacts cannot be avoided, but self-excited fluctuations must be controlled. As indicated in the previous section, tooth error is the main cause of these fluctuations, the magnitudes of which are weakened by the existence of backlash clearance. The effects of backlash clearance size and tooth error size are thoroughly discussed in this section.

4.1. Influence of backlash clearance size

Backlash clearance, which is micron-scaled, has been verified to have a limited influence on rotational precision. The error of angular displacements can be neglected when the backlash clearance is $100\,\mu$ m and 6 mm. The latter value is nearly one-third of the tooth thickness, which is considered an extreme value in the actual design. The positioning error stays in a 0.001 rad scale. The final error eventually converges to zero, particularly for a closed-loop controlling method.

However, the displacement error will accumulate if the links are repeatedly driven back and forth. Figure 15 shows the accumulated error when both joints are driven by torque $T = 2000\sin(20\pi\sqrt{t})$. The error apparently increases with the increase in the backlash size. Space manipulators rarely work
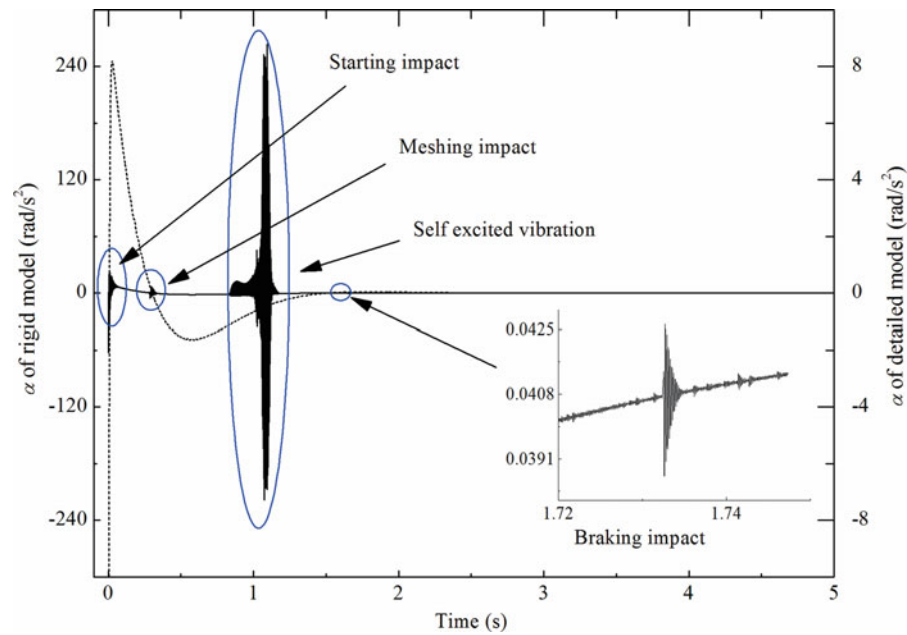
Fig. 14. Angular acceleration of the shoulder joint in the first 1.2 s; the dashed line is the rigid model, whereas the solid line is the detailed model.
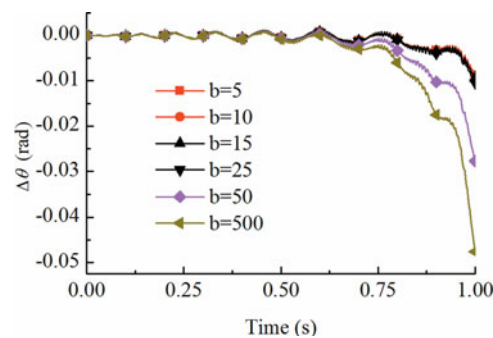

Fig. 15. Accumulated error of the shoulder joint when rotating back and forth.

under such critical circumstance. Moreover, a closed-loop controlling method with encoder feedback will erase the error every time the links rotate backwards. Therefore, the backlash clearance error also accumulates when the manipulator repeatedly goes back and forth, which rarely happens in actual situations.

As discussed in the previous section, the backlash size produces a strong effect on the fluctuation magnitude. To study such phenomenon, a set of different backlash clearance models is simulated, in which parameter b is set to 5, 10, 25, 50, 500, 1000, and 3000 μ m. Figures 16 and 17 show the results of the shoulder joint sun-planet meshing force during the meshing and self-excited impacts. Although an increase in the backlash clearance size enhances the severity of the meshing force impact, such impact occurs at a later time and in a shorter duration because a larger clearance requires more time to re-contact when the gear pair changes its contacting side.

The result in Fig. 17 is similar to that presented in the previous section, which was derived when the backlash clearance is set to zero. The fluctuation magnitude of the internal excitation obviously recedes when the backlash clearance size increases. A smaller backlash clearance causes a small-range gear pair vibration, and the contact of the adjacent pair changes the meshing side back and forth, which results in continuous excitation. Therefore, the size of backlash clearance is not the smaller the better, and a suitable backlash clearance size is the key to suppressing severe fluctuation.

Figure 18 shows the FFT analysis results of the joint angular accelerations during self-excited fluctuation. The fundamental frequency of the fluctuation is approximately 1500 Hz, and several
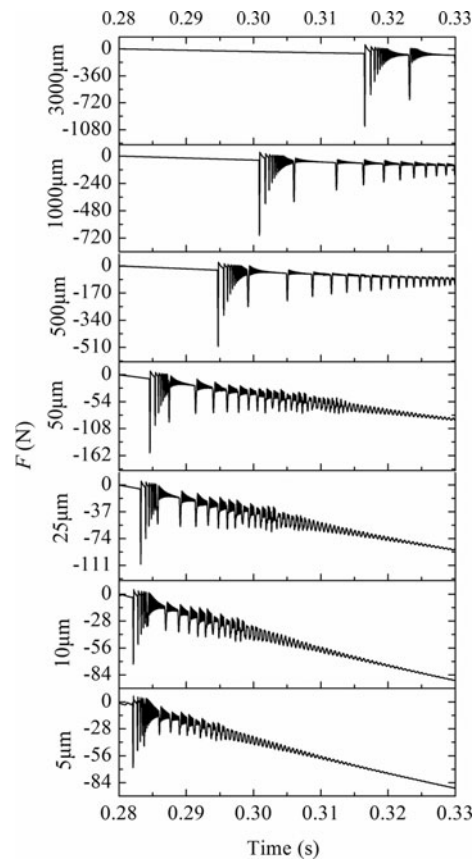
Fig. 16. F_{sp1} of different clearances during impact.

doubling frequencies also appear. The magnitude of the elbow joint acceleration is much greater than that of the shoulder joint because the motion of the first link is coupled with that of the second link. The fundamental frequency drifts into the low frequency stage as the clearance size increases. A chaotic fluctuation is observed when the backlash clearance increases to a value larger than $500\,\mu$ m, and the FFT result is a continuous spectrum in the low frequency area. Given that the meshing impact is also affected by the backlash clearance, neither an oversized nor undersized backlash clearance is considered suitable for attaining a steady transmission. A backlash clearance of approximately $50\,\mu$ m is deemed suitable for the simulated system in this study.

4.2. Influence of the tooth profile error

Tooth profile error is mainly composed of surface roughness error and manufacturing error. Given that the gear surface is usually machined by ground finish, the roughness error is generally micron-scaled. Manufacturing errors include misaligned work pieces or cutters as well as measurement errors, which are controllable. Therefore, a tooth error magnitude of $10\,\mu$ m is considered extreme to a certain degree. The tooth errors of 1.6, 3.2, 5, and $6.3\,\mu$ m are simulated in this section. The tooth error size barely affects positioning error, which is not difficult to explain. The error size, which basically includes irregularities in the tooth surface profile, is smaller than the backlash size by one order of magnitude. The angular displacement error is mostly unchanged when the tooth error increases. The meshing and starting impacts rapidly converge when the backlash clearance grows larger than the error magnitude and the impact energy release after tooth surface deformation. Therefore, these results are not displayed in this article, and this section mainly focuses on the self-excited fluctuation that is caused by tooth error.

Figure 19 shows the highly remarkable influence of error size on the self-excited fluctuation. The internal excitement is not strong enough to excite a fluctuation when the tooth error size is smaller
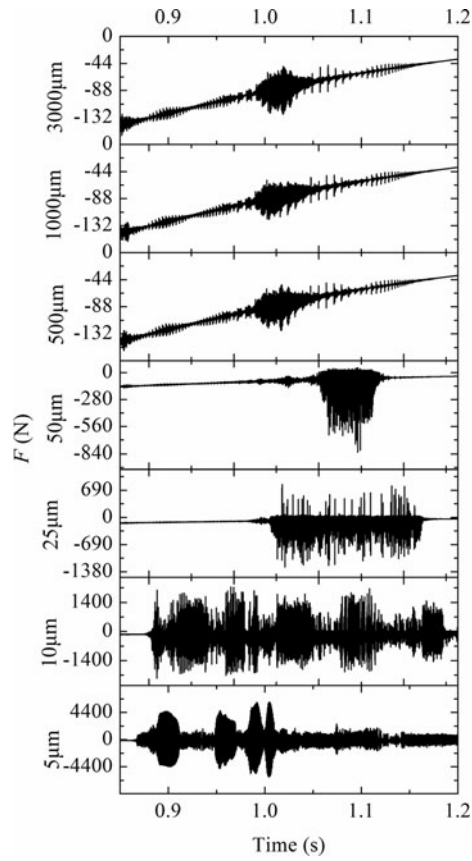
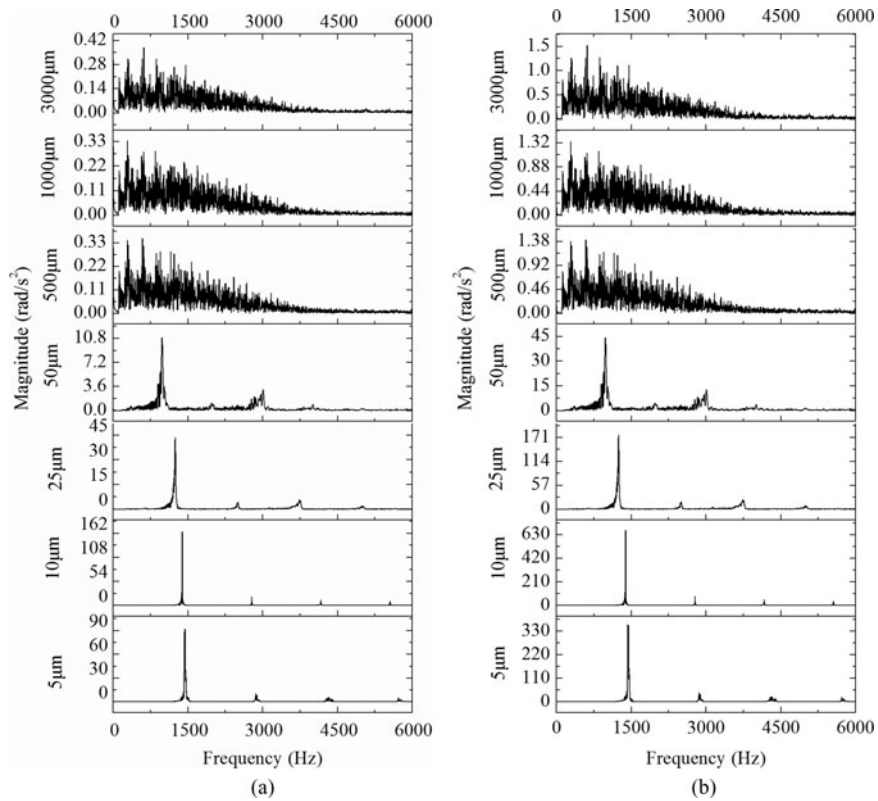Fig. 17. F_{sp1} of different clearances during self-excited fluctuation.

Fig. 18. (a) Shoulder joint and (b) elbow joint angular acceleration in the frequency domain.
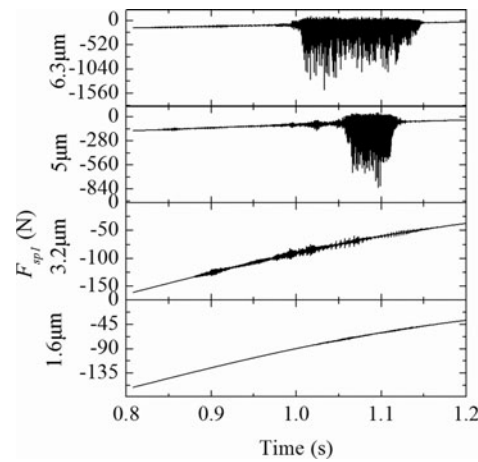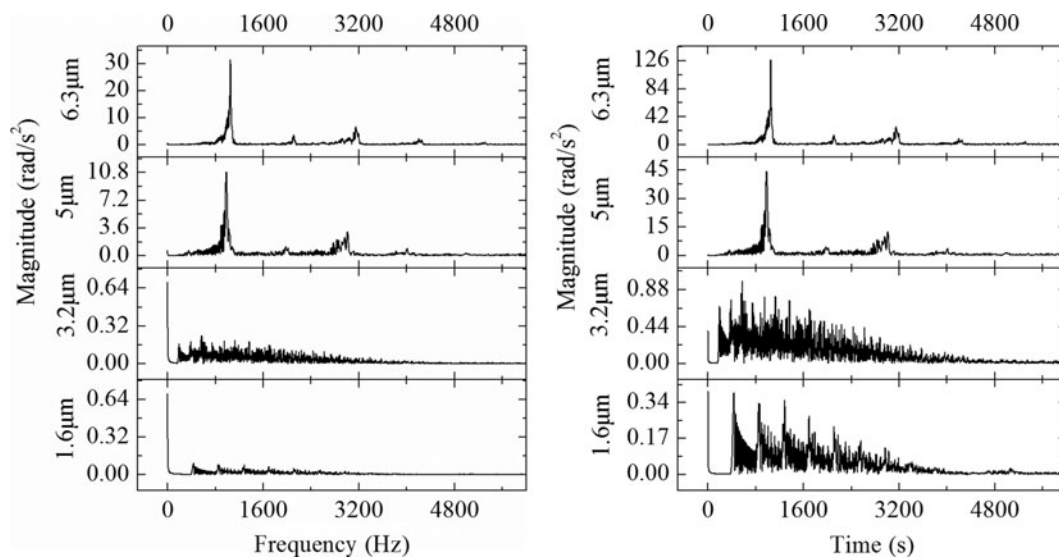
Fig. 19. F_{sp1} during self-excited fluctuation.

Fig. 20. (a) Shoulder joint and (b) elbow joint angular acceleration in the frequency domain.

than $1\,\mu$ m, whereas minor fluctuations appear when the error size reaches $1.6\,\mu$ m. The meshing contact force evidently increases when the error becomes larger.

Joint acceleration is analyzed in frequency domain as illustrated in Fig. 20. The shoulder joint displays a 0 Hz magnitude, which represents the rigid rotation of the joint, and some chaotic high-frequency components, which represents a minor fluctuation, when the tooth error is less than $5\,\mu$ m. The high-frequency component magnitude of the elbow joint is larger compared with the 0 Hz component because the fluctuation of link 1 is transmitted to the elbow joint. The self-excited fluctuation becomes more observable when the tooth error is greater than $5\,\mu$ m. The composed components are basically the same as those that are shown in Fig. 18. Given that the magnitude dramatically increases even when the error only increases by $1.3\,\mu$ m, the tooth error is identified as the reason behind the occurrence of self-excited impacts, and tiny errors will result in tremendous fluctuations.

5. Conclusion
A new model for a two-link space manipulator system is developed in this study. The manipulator joint is transmitted through a planetary gear train, and the detailed model of the 2K-H planetary gear train is completed. The backlash clearance, gear tooth error, and time-variant meshing stiffness are

all considered in the model. Examples of the constant torque driving and PD driving method are simulated. Gear meshing results in fluctuation during processing, and backlash clearance is the cause of excitation. The fluctuation magnitude becomes more severe when the backlash clearance increases. The tooth error results in a self-excited fluctuation, whereas a small backlash clearance intensifies such fluctuation. Given that backlash clearance is unavoidable in the planetary gear train, a suitable backlash size is needed in the system and the tooth profile error must be kept as small as possible to enhance manufacturing precision.

Acknowledgements

References

1. S. Yu and M. A. Elbestawi, "Modelling and dynamic analysis of a two-link manipulator with both joint and link flexibilities," *J. Sound Vib.* **179**(5), 839–854 (1995).
2. G. Gibbs and S. Sachdev, "Canada and the international space station program: overview and status," *Acta Astronautica* **51**(1–9), 591–600 (2002).
3. J. J. Yu, J. S. Dai, T. S. Zhao, S. S. Bi and G. H. Zong, "Mobility analysis of complex joints by means of screw theory," *Robotica* **27**, 915–927 (2009).
4. T. Komatsu, M. Uenohara, S. Iikura, H. Miura and I. Shimoyama, "Dynamic control for two-link flexible manipulator," *Nippon Kikai Gakkai Ronbunshu, C Hen/Trans. Japan Soc. Mech. Eng. C* **55**(516), 2022–2028 (1989).
5. A. S. Morris and A. Madani, "Static and dynamic modelling of a two-flexible-link robot manipulator," *Robotica* **14**(pt 3), 289–300 (1996).
6. B. He, F. Gao and S. Wang, "Modeling and simulation of a mechanical arm with joint clearance," *J. Tianjin Univ. Sci. Technol.* **38**(9), 795–799 (2005). (In Chinese)
7. P. K. Nguyen, R. Ravindran, R. Carr, D. M. Gossain and K. H. Doetsch, "Structural Flexibility of the Shuttle Remote Manipulator System Mechanical Arm," *Proceedings of the Guidance and Control Conference*, San Diego, CA, USA (1982) pp. 246–256.
8. M. W. Spong, "Modeling and control of elastic joint robots," *J. Dyn. Syst., Meas. Control* **109**(4), 310–318 (1987).
9. F. Ghorbel, J. Y. Hung and M. W. Spong, "Adaptive Control of Flexible-Joint Manipulators," *Proceedings of the 1989 IEEE International Conference on Robotics and Automation,* Scottsdale, AZ, USA (May 14–19, 1989) pp. 9–13.
10. M. H. Korayem and A. Nikoobin, "Maximum payload for flexible joint manipulators in point-to-point task using optimal control approach," *Int. J. Adv. Manuf. Technol.* **38**(9–10), 1045–1060 (2008).
11. H. Salmasi, R. Fotouhi and P. N. Nikiforuk, "A biologically inspired controller for trajectory tracking of flexible-joint manipulators," *Int. J. Robot. Autom.* **27**(2), 151–162 (2012).
12. L. Hong, Y. Liu, J. Minghe, K. Sun and J. B. Huang, "An experimental study on Cartesian impedance control for a joint torque-based manipulator," *Adv. Robot.* **22**(11), 1155–1180 (2008).
13. M. K. Ciliz, "Adaptive control of robot manipulators with neural network based compensation of frictional uncertainties," *Robotica* **23**(2), 159–167 (2005).
14. B. Subudhi and A. S. Morris, "Singular perturbation based neuro-H-infinity control scheme for a manipulator with flexible links and joints," *Robotica* **24**(2), 151–161 (2006).
15. J. Zhao and C. Fang, "On the joint velocity jump during fault tolerant operations for manipulators with multiple degrees of redundancy," *Mech. Mach. Theory* **44**(6), 1201–1210 (2009).
16. J. Zhao and Q. Li, "On the joint velocity jump for redundant robots in the presence of locked-joint failures," *J. Mech. Des.* **130**(10230510), (2008).
17. J. Zhao and S. Bai, "The study of coordinated manipulation of two redundant robots with elastic joints," *Mech. Mach. Theory* **35**(7), 895–909 (2000).
18. D. M. Gan, N. G. Tsagarakis, J. S. Dai, D. G. Caldwell and L. D. Seneviratne, "Stiffness design for a spatial 3-DOF compliant manipulator based on impact configuration decomposition," *Trans. ASME, J. Mech. Robot.* **5**(1), 2013, pp. 011002(1–10).
19. Y. Woosoon, "Adaptive Control of a Flexible Joint Manipulator," *Proceedings of the 2001 ICRA. IEEE International Conference on Robotics and Automation,* Seoul, South Korea (2001) pp. 3441–3446.
20. Z. Du, Y. Xiao and W. Dong, "Modeling of robot joints with friction, backlash and hysteresis," *Robot* **33**(5), 539–545 (2011). (In Chinese)
21. B. O. Al-Bedoor and A. A. Almusallam, "Dynamics of flexible-link and flexible-joint manipulator carrying a payload with rotary inertia," *Mech. Mach. Theory* **35**(6), 785–820 (2000).